Tunneling magnetoresistance in all-antiferromagnetic Mn_2 Au-based tunnel junctions

Xintao Jia [1,*] Hui-Min Tang [2,†] and Shi-Zhuo Wang [3]

[1] *School of Physics and Electronic Information Engineering, Henan Polytechnic University, Jiaozuo 454000, China*

[2] *School of Physical Science and Technology, Guangxi Normal University, Guilin 541001, China*

[3] *School of Physics and Electronic Engineering, Zhengzhou University of Light Industry, Zhengzhou 450002, China*

(Received 15 March 2023; revised 23 August 2023; accepted 25 August 2023; published 5 September 2023)

Antiferromagnetic (AF) spintronics offers the advantages of ultrahigh operating speed and stability to a device in the presence of a magnetic field. To fully exploit these advantages, the device should be comprised of all-AF materials. Although achieving a noticeable magnetoresistance (MR) effect in an all-AF device is difficult, this effect is essential for AF spintronic applications. Herein, we investigated the tunneling MR (TMR) effect in all-AF Nb/Mn_2Au/CdO/Mn_2Au/Nb magnetic tunnel junctions (MTJs) using first-principles scattering theory. Through calculations, we predicted the presence of high TMR, which was found to be of the order of 1000% in the case of some symmetric junctions. This could be attributed to the interfacial resonance-tunneling effect related to the $k_{||}$-dependent complex band structures of CdO and Mn_2Au and to the high spin polarization of the interfacial magnetic atoms. Moreover, we studied the effects of voltage bias and interfacial disorder, such as oxygen vacancies, manganese vacancies, and manganese–cadmium exchanges, at the Mn_2Au/CdO interface. Our findings indicate that all-AF Nb/Mn_2Au/CdO/Mn_2Au/Nb MTJs are highly promising materials for spintronic applications and that rocksalt CdO is a potential symmetry-filtering material for such applications.

DOI: 10.1103/PhysRevB.108.104406

I. INTRODUCTION

Antiferromagnetic (AF) spintronics has emerged as a promising candidate for next-generation electronics due to the ultrahigh-speed spin dynamics (up to THz) of the involved materials and their insensitivity to magnetic fields [1,2]. These properties render AF spintronics promising for various applications, such as magnetic memories, magnetic sensors, and brain-inspired computations. To fully leverage the benefits of AF spintronics, avoiding the use of ferromagnets (FMs) and ferrimagnets as references or pinning layers is crucial. Magnetoresistance (MR) is usually evident in magnets, with the nonrelativistic MR effect being always larger than the relativistic one. However, the MR effect in AF spin valves (SVs) [3] is fundamentally different from that in ferromagnetic ones, and it is generally too small to meet the commercial requirements [1,2]. Recently, several schemes were proposed to improve the MR effect in AF devices. The use of perfect spin-filtering materials, hybrid magnetic tunnel junctions (MTJs) with FMs as the spin polarizer and antiferromagnets (AFMs) as the active layer, can enhance the tunneling MR (TMR) effect by >700% [4,5]. A large MR effect (>7000%) can be found in certain sandwich-type van der Waals (vdW) junctions with synthetic AF structures, which is related to the magnetic state-dependent band structure [6–11]. Yang *et al.* experimentally studied unconventional colossal angular MR (AMR) in the semiconductor-type AFM $EuTe_2$ with a broken space-time inversion symmetry [12], which is related to the metal-insulator transition induced by magnetic fields. Dong *et al.* predicted large TMR (as high as 300%) in all-AF Mn_3Sn-based MTJs [13], originating from spin splitting in the momentum space. This scheme was recently experimentally demonstrated by Qin *et al.* [14]. Šmejkal *et al.* predicted giant MR (GMR) and TMR of approximately 100% in all-AF RuO_2-based MTJs [15], which was attributed to spin-momentum coupling.

The use of electric current is the preferred method for manipulating AFMs [1,2,16,17]; this method is compatible with state-of-the-art semiconductor technology. When current flows through an AF metal with broken inversion symmetry, the Néel spin-orbit torque (NSOT) [18–21] or spin-orbit torque (SOT) [22] can switch the Néel order with a current density of as low as 10^6 A/cm^2, which is comparable to the current-induced spin-transfer torque (STT) in well-studied MgO-based ferromagnetic tunnel junctions (F-MTJs) [23–25]. The spin Hall effect (SHE) can be induced in a noble metal by passing current through it; this effect can then be used to manipulate AFMs [26]. The antidamping spin torque induced by this effect can switch the Néel order of tetragonal Mn_2Au [27]. Although the electronic current for switching the AFM using the SHE effect is large [26], it can be considerably reduced by exploiting the topological surface states [28].

The spin dynamics of AFMs can be described using the coupled Landau-Lifshitz-Gilbert equation [1,2], with the timescale depending on the exchange field of the magnetic moments. Notably, the spin dynamics of synthetic AFMs are notably different from those of intrinsic AFMs but similar to those of ferromagnetic SVs. Although synthetic two-dimensional (2D) AFMs can exhibit a large MR effect [6–10], they cannot be considered as all-AF spintronic devices. Up to now, reports on the MR effect in an all-AF device have

*Corresponding author: jiaxingtao@hpu.edu.cn

†Corresponding author: hmtang@gxnu.edu.cn

been rare. Therefore, it is essential and urgent to explore the all-AF device with noticeable MR effects and good compatibility with state-of-the art semiconductor architecture for AF spintronic applications.

The sizable MR effect in clean Fe/MgO/FeMn [5] and Fe/MgO/Mn_2Au [4] AF-MTJs is believed to be related to localized interfacial states. Thus, it is essential to ensure that the interfaces are clean, as interfacial disorders such as atomic and spin disorder can destroy the interfacial states. To achieve ideal interfaces, it is favorable to have epitaxial contact between the AF metal and nonmagnetic material. In this study, we focus on epitaxial Mn_2Au/CdO/Mn_2Au all-AF MTJs with ideal interfaces. Tetragonal Mn_2Au has a high Néel temperature above 1000 K [29], and the current-induced NSOT effect can manipulate the Néel vector efficiently [18]. Cubic CdO shows a rocksalt (NaCl) structure with lattice parameter $a = 4.69$ Å, which can match well with the tetragonal Mn_2Au by a 45° rotation. The current-induced STT is not so efficient in manipulating the Néel order of the tetragonal Mn_2Au [26]. A three-terminal structure using NSOT or the SHE effect is more favorable. In these cases, the Mn_2Au layer should be as thin as possible. bcc Nb or Ta with lattice parameter $a = 3.3$ Å can be used as a lead, which can match well with Mn_2Au, the former being more cost-effective.

II. METHODS

In this study, a two-terminal structure consisting of Mn_2Au/CdO/Mn_2Au sandwiched between two semi-infinite Nb leads was used to investigate the MR effect. The stacking of the Mn_2Au/CdO/Mn_2Au multilayer is shown in Fig. 1. First, we carried out density functional theory (DFT) calculations based on the plane-wave function to determine the stable structure. Then we performed tight-binding linear muffin-tin orbital (TB-LMTO) calculations to obtain the potentials of the system. Finally, we transferred the potentials into a wave-function-matching (WFM) package to calculate the spin transports.

A. Device structure and ground-state calculations

We carried spin-dependent first-principles calculations based on DFT with the generalized gradient approximation (GGA) parametrized as the Perdew-Burke-Ernzerhof (PBE) exchange-correlation functional and the projector augmented wave (PAW) approach [30] to find stable structures. A slab structure containing six layers of CdO and six layers of Mn_2Au is used to study the Mn_2Au/CdO(001) interface. In the calculations, we expanded CdO to match with Mn_2Au. Moreover, all parameters were fixed to the bulk state, with the only free parameter being the distance between Mn_2Au and CdO. A cutoff energy of 600 eV was used for all the calculations. These calculations indicated that the cases of O termination for CdO were stable with regard to energy. The total energies of the structures with the bonds of the Au, Mn1, and Mn2 of Mn_2Au (Fig. 1) with the O of CdO (approximate bonding lengths being 2.41, 2.03, and 1.93 Å, respectively) were −129.092, −130.038, and −130.047 eV, respectively, while the formation energies E_{int} were −0.502, −1.436, and −1.469 eV, respectively. The formation energies were

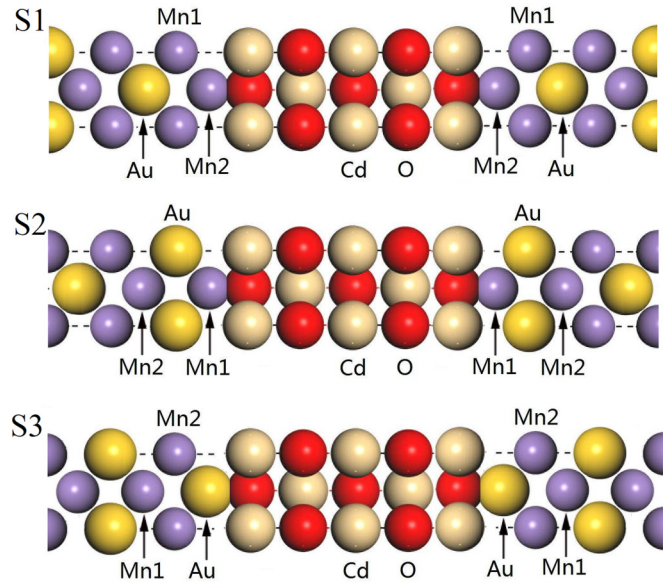

Mn_2Au structure contacted with CdO		Structure
Left-side	Right-side	
...AuMn1Mn2	Mn2Mn1Au...	S1
...Mn2AuMn1	Mn1AuMn2...	S2
...Mn1Mn2Au	AuMn2Mn1...	S3
...Mn1Mn2Au	Mn2Mn1Au...	A1
...Mn1Mn2Au	Mn1AuMn2...	A2
...AuMn1Mn2	Mn1AuMn2...	A3

FIG. 1. Schematic of the Mn_2Au/CdO/Mn_2Au (001) multilayer used in the present study. It is important to consider the crystal structure and termination atoms of the AFM. Based on the termination atoms of Mn_2Au in contact with CdO, we have defined three symmetric structures (S1, S2, and S3) and three asymmetric structures (A1, A2, and A3). For notation, we identify the left side of Mn_2Au from left to right but its right side from right to left. Consequently, the left side of Mn_2Au follows an ...ABCABC... structure, while its right side follows a ...CBACBA... structure. For the left side of Mn_2Au, A, B, and C stand for Au, Mn right-contacted with Au (Mn1), and Mn right-contacted with Mn1 (Mn2), respectively.

calculated using the following equations: $E_{\text{int}} = E_{\text{CdO/Mn}_2\text{Au}} - (E^{\text{slab}}_{\text{CdO}} + E^{\text{slab}}_{\text{Mn}_2\text{Au}})$, where $E_{\text{CdO/Mn}_2\text{Au}}$, $E^{\text{slab}}_{\text{CdO}}$, and $E^{\text{slab}}_{\text{Mn}_2\text{Au}}$ were the total energies of the CdO/Mn_2Au surface, the CdO slab, and the Mu_2Au slab, respectively. Herein, the structures above were denoted as "Au termination," "Mn1 termination," and "Mn2 termination," respectively. Therefore, the most energy-favorable interface was the Mn_2Au/CdO interface with the Mn2 termination structure. For the Nb/Mn_2Au interface, DFT calculations indicated that the structure with Mn (of the Mn_2Au layer) situated above the second-monolayer Nb (of the Nb layer) was more energy favorable. The magnetic moments of the three interfaces are shown in Table I. Therein, the magnetic moments of Mn atoms closest to the CdO region are significantly enhanced compared with about 3.68 μ_B of Mn atoms in bulk Mn_2Au; the noticeable difference indicates that there are considerable differences in the spin transports.

TABLE I. The magnetic moments (in units of μ_B) of the Mn1 and Mn2 atoms of the three interface structures.

	S1	S2	S3
Mn1	−3.79	3.99	−3.65
Mn2	3.83	−3.61	3.73

The potentials used in the transport package in this study were obtained through self-consistent spin-dependent DFT calculations using the TB-LMTO surface Green's function method, and a coherent potential approximation was used to deal with potential imperfections [31]. Notably, the atomic radius of Nb was 1.639 Å, resulting in the complete filling of the bcc lattice. For Mn_2Au, the same atomic radius of 1.555 Å was used for both Au and Mn to fill the tetragonal lattice. For CdO, radii of 1.492 and 1.237 Å were used for O and Cd, respectively, and an empty sphere with a radius of 0.796 Å was added to the center of the cube comprising four O and four Cd atoms to fill the space. Using the modified Becke-Johnson (mBJ) [32] potential within the local spin density approximation, we found that the direct band gap of CdO at the Γ point was approximately 2.85 eV. The conduction-band minimum (CBM) was approximately 1.3 eV above the Fermi energy, while the indirect band gap was approximately 1.5 eV, with the valance-band maximum (VBM) localized at the L (0.5 0.5 0.5) point [Fig. 3(b)]. The band structure was consistent with those reported in previous studies [33,34]. For the Mn_2Au/CdO interface, three empty spheres were introduced to fill the space during self-consistent spin-dependent DFT and spin-transport calculations. Two empty spheres with a radius of r_1 were inserted exactly above the empty spheres inside CdO, and an empty sphere with a radius r_2 was inserted exactly above Cd. The former spheres were considered to belong to the CdO layer, and the position of the latter sphere was arranged to minimize any overlap. For the Mn2 termination structure, both r_1 and r_2 were set to 0.653 Å. For the Mn1 termination structure, r_1 and r_2 were set to 0.796 and 0.668 Å, respectively. For the Au termination structure, r_1 and r_2 were set to 0.796 and 0.956 Å, respectively.

B. Transport calculations

Herein, spin-transport calculations were performed using the first-principle WFM method [35] for ideal junctions. When interfacial disorders were present, vertex correction [36] was used to average the configurations. The Néel order vector **n** of Mn_2Au was determined based on the magnetic moment direction of the first Mn atom that came in contact with CdO. The left-side Néel order $\mathbf{n}_L$ was fixed as a reference, while the right-side Néel order $\mathbf{n}_R$ was set free. To ensure good numerical convergence for ideal epitaxial structures, a $1600 \times 1600k$-mesh was utilized to sample the 2D Brillouin zone (BZ) for most structures. The electron affinity and work function of CdO and Mn_2Au slab were 3.4 and 4.5 eV, respectively, resulting in a Schottky barrier height of approximately 1.1 eV of the Mn_2Au/CdO interface. The band structure of CdO at the center of the barrier [considering that these atoms follow a three-dimensional (3D) periodic structure] was almost the same as that of the bulk material, with a small deviation in the position of the Fermi level. However, the band structure of CdO that was in contact with the Mn_2Au layer was considerably different from that of the bulk material.

III. RESULTS AND DISCUSSION

First-principles spin-dependent DFT calculations indicated that the Mn_2Au/CdO interface with the Mn2 termination structure, which was the focus of the present study, was the most energetically stable interface. Comparatively, the Au and Mn1 termination structures were less stable; however, their presence might be experimentally confirmed under certain conditions. Figure 1 illustrates six possible structures in the Mn_2Au/CdO/Mn_2Au multilayer, with the S1 structure being the most energetically favorable and the primary focus of this study. The tetragonal Mn_2Au exhibited fourth-order in-plane anisotropy with a hard axis along the z direction and an easy axis maybe along $\theta = 90^\circ$, $\phi = \pm 45$, or $\pm 135^\circ$ [37]. The relative angle Θ between the Néel vector of the reference (left) side ($\mathbf{n}_L$) and the free (right) side ($\mathbf{n}_R$) defined three stable magnetic states—parallel (P), perpendicular (PP), and antiparallel (AP) states—corresponding to $\Theta = 0$, $\pi/2$, and π, respectively. For example, the P state was defined when the magnetic moments of the left-side Mn1 and Mn2 atoms of the S1 structure were along $\theta = 90^\circ$, $\phi = 45^\circ$ and $\theta = 90^\circ$, $\phi = -45^\circ$, respectively, and the magnetic moments of the right-side Mn2 and Mn1 atoms of the S1 structure were along $\theta = 90^\circ$, $\phi = -45^\circ$ and $\theta = 90^\circ$, $\phi = 45^\circ$, respectively. Furthermore, we defined the angular-dependent TMR as $\mathrm{TMR}(\Theta) = R(\Theta)/R(0) - 1$ with resistance $R = 1/G$ and conductance $G = (e^2/\mathrm{h})\mathrm{Tr}(tt^\dagger)$, where t is the transmission part of the scattering matrix S.

A. TMR in AF MTJs

Figures 2(a) and 2(b) demonstrate the spin transmissions and TMRs in the ideal all-AF Nb/Mn_2Au(12-120)/CdO(4-20)/Mn_2Au(12-120)/Nb MTJs with an S1 structure, where the numbers in the parentheses denote the thickness in atomic layers (Ls). These junctions were referred to as the Nb-lead junctions because they use Nb leads. Initially, we varied the thickness of Mn_2Au while keeping that of CdO fixed at 10 Ls [Fig. 2(a)]. Therein, the spin transmissions of the AP structure were less sensitive to the thickness of the Mn_2Au region, which was approximately one order of magnitude smaller than the spin transmissions of the much thicker Mn_2Au junction (referred to as the Mn_2Au-lead junction). The spin transmissions of the AF MTJs with P and PP magnetic states initially increased and then decreased, with peak values around 18-Ls Mn_2Au. These peak values were almost three times larger than those of the junction with 120-Ls Mn_2Au, and approximately one order of magnitude larger than those of the Mn_2Au-lead junction. Considering the metallicity of tetragonal Mn_2Au, the sensitivity of the spin transmission in the AF MTJs with respect to the Mn_2Au thickness was unusual [4]. The TMR studies indicated huge TMRs ranging from 1600% to 5600% in the AF MTJs as Mn_2Au varied from 12 to 120 Ls, which were approximately one order of magnitude larger than that of the Mn_2Au-lead junction [Fig. 2(a)]. These TMRs were comparable to the specular TMR effect found in the well-studied MgO-based F-MTJs [23,24,38,39]. Furthermore,

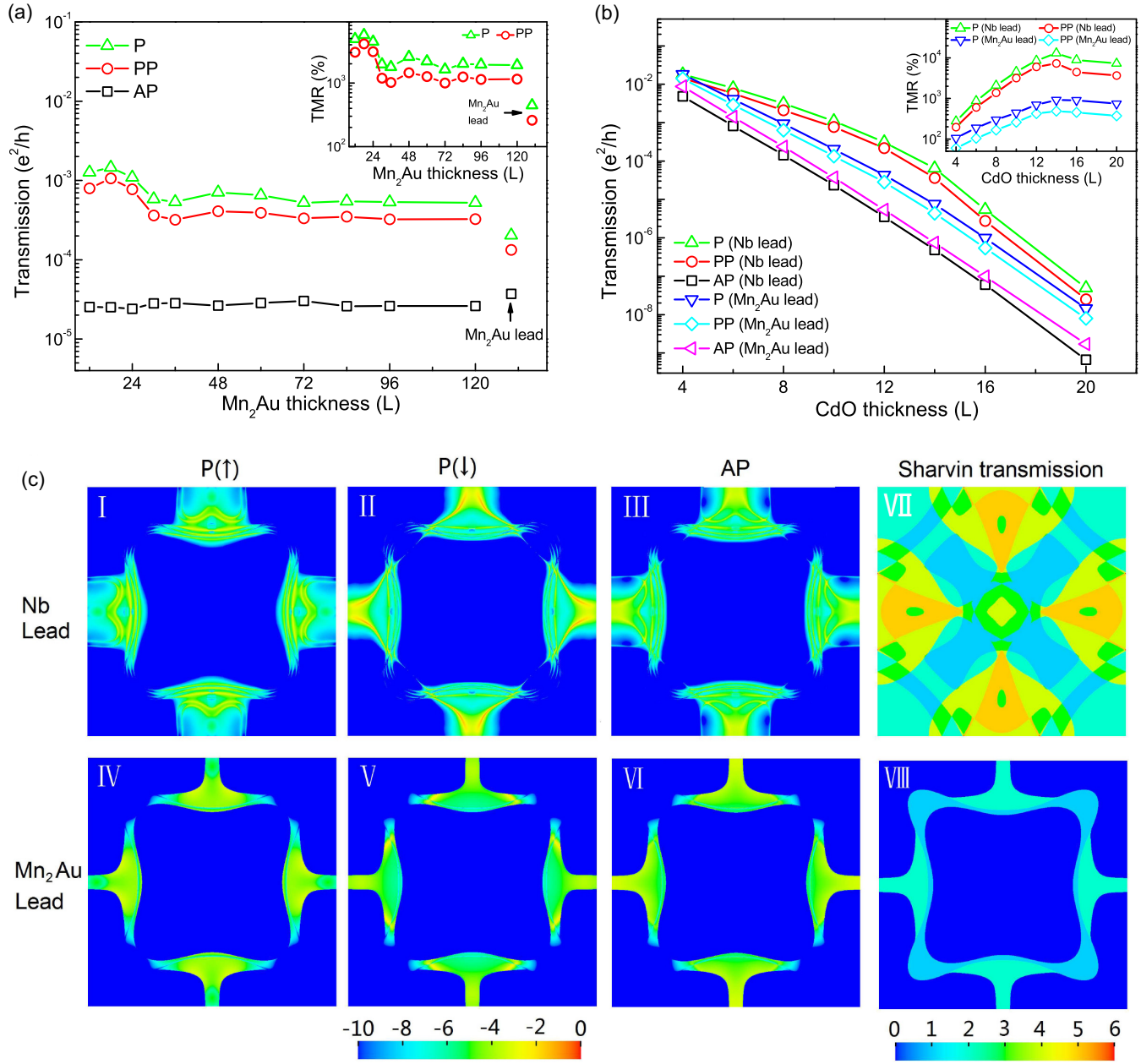

FIG. 2. (a) Mn_2Au thickness dependency and (b) CdO thickness dependency of the spin transmissions and TMRs of the ideal Nb/Mn_2Au/CdO/Mn_2Au/Nb and Mn_2Au/CdO/Mn_2Au all-AF-MTJs with S1 structure. The CdO barrier thickness is set 10 Ls in (a), and both the reference and free Mn_2Au layers are set 24 Ls in (b) for the "Nb lead" junctions. (c) $k_{||}$-resolved transmission coefficient in the 2D BZ of the ideal (I-III) Nb/Mn_2Au(24)/CdO(10)/Mn_2Au(24)/Nb(001) and (IV-VI) Mn_2Au/CdO(10)/Mn_2Au(001) all-AF-MTJs with S1 structure at Fermi energy, and Sharvin transmission of (VII) bcc Nb and (VIII) tetragonal Mn_2Au along the [001] direction.

the spin transmission of the AF MTJs followed simple trigonometric functions, and the TMR effect of the PP magnetic states was approximately 50% of that of the P states (Table II).

Spin transmissions in both Nb and Mn_2Au-lead AF MJTs exhibited an exponential decrease with increasing thickness of the CdO barrier. Notably, when the barriers were thinner, there was a considerable deviation in spin transmissions of the P and PP magnetic states [Fig. 2(b)]. In calculations, the Mn_2Au thickness for the Nb-lead junctions was fixed at 24 Ls. Both types of junctions initially demonstrated a rapid increase in TMRs as the CdO thickness increased, followed by a slower increase until a peak was reached at approximately 14-Ls CdO thickness, after which the TMR gradually decreased. In P magnetic state junctions, the smallest and largest TMRs were 270% (in the junction with 4-Ls CdO) and 13 000% for the Nb-lead junctions and 105% and 920% for the Mn_2Au-lead junctions, respectively. When the CdO barrier was thicker, the TMRs of the Nb-lead junctions were approximately one order of magnitude larger than those of the Mn_2Au-lead junctions. This notable disparity implies the presence of a spin-filtering effect in the Nb-lead junctions.

TABLE II. Tunneling conductances and TMRs of the ideal Nb/Mn_2Au(24)/CdO(10)/Mn_2Au(24)/Nb(001) AF-MTJs at zero and 0.1 eV (in the parentheses) voltage bias. The unit of conductance is 10^{-5} e^2/h.

Structures	P	AP	PP	TMR(P) (%)	TMR(PP) (%)
S1	110(3.96)	2.35(2.20)	77.2(3.16)	4580(80)	3180(44)
S2	4.28(1.36)	0.180(0.101)	2.27(0.737)	2270(1250)	1160(536)
S3	0.925(0.0667)	0.011(0.0191)	0.49(0.0429)	8300(250)	4350(125)
A1	0.468(0.0369)	0.279(0.0230)	0.375(0.0301)	68(60)	34(31)
A2	0.0583(0.0250)	0.0348(0.0136)	0.0466(0.0199)	67(84)	34(46)
A3	0.967(1.55)	0.68(0.755)	0.773(1.19)	42(105)	14(57)
S1[a]	9.15	2.59	5.89	252	127
S1[b]	28.9	12.9	20.98	123	63
S1[c]	10.4	2.61	6.51	298	149

[a]10% Oxygen vacancies at both Mn_2Au/CdO interfaces.
[b]10% Manganese vacancies at both Mn_2Au/CdO interfaces.
[c]10% Manganese-cadmium (Mn-Cd) exchanges at both Mn_2Au/CdO interfaces.

According to the two-current model, the current flowing through a potential barrier should be spin-polarized to induce the MR effect. In the nonrelativistic case limit, the current flowing through the AF metal Mn_2Au is hard to spin-polarize. However, the calculations of spin transmissions and TMRs presented above indicate that the Mn_2Au layers are almost half-metallic, a fact that might be related with the interface effect noted in Fe/MgO/Ag/Mn_2Au [4] hybrid AF MTJs.

Figure 2(c)(I–III) provides the $k_{||}$-resolved spin transmissions of ideal Nb/Mn_2Au(24)/CdO(10)/Mn_2Au(24)/Nb AF MTJs with S1 structure at the Fermi energy. In the P (AP) magnetic state of the Nb-lead junctions, the sum of the $k_{||}$-resolved spin transmission of the majority (↑) and minority (↓) spins is 5.75(0.116) × 10^{-4} e^2/h and 2.29(0.117) × 10^{-4} e^2/h, respectively. The difference between the ↑ and ↓ spin transmission of the AP magnetic state junction is within the error bar of our calculations, and the total $k_{||}$-resolved transmissions are shown in Fig. 2(c). Current spin polarization around 43% of the P magnetic state junction suggests that the existence of large TMR is considerably different from that in the ideal MgO-based F-MTJs, where transmission is close to 100% spin-polarized [23]. Upon examining the 2D BZ [Fig. 2(c)(I) and (II)], it is evident that the hot spots and hot lines dominate the total transmission for both spin channels. In addition, they are highly spin-polarized and located in different regions. The sum of resonant $k_{||}$ points with a transmission possibility larger than 0.01 contributes to approximately 94% and 40% of the total transmission of P and AP magnetic states, respectively, of the Nb-lead junction. Additionally, approximately one-fourth of the 2D BZ contributes to the Sharvin conductance of bulk Mn_2Au at the Fermi energy, as shown in Fig. 2(c)(VIII), indicating that Mn_2Au can serve as a $k_{||}$-resolved potential barrier material. We name this region the Sharvin area, which can be well-understood by the band structure [Fig. 3(a)] and Fermi surface [Fig. 3(d)(I)] of bulk Mn_2Au along the transport direction. Furthermore, the $k_{||}$ points out of the Sharvin area of Mn_2Au contribute approximately 67% and 7% of the total transmission for the ↑ and ↓ spin of the P magnetic state, respectively, but less than 1% for both spin channels of the AP state. The resonance $k_{||}$ points within and outside of the Sharvin area of Mn_2Au show differences in details. Both bonding and antibonding peaks (with an energy gap around 10^{-1} eV) of the former are splitting further into two peaks with an energy gap around 10^{-4} eV, which could be attributed to the complex coupling of the interfacial states.

Figure 2(c)(IV–VI) presents the $k_{||}$-resolved spin transmissions of the Mn_2Au-lead junctions. Similar to the Nb-lead junctions, the bright areas of the ↑ and ↓ spin channels of the P magnetic state of the junction are located in different regions of 2D BZ, and the spin transmission is not only spin- but also $k_{||}$-dependent. The sum of spin transmissions of the P magnetic state junction results in a spin polarization of 9% in comparison to approximately 43% in the Nb-lead junction.

B. Band-structure analysis

Núñez *et al.* [3] proposed a theoretical model to estimate the MR effect in L-type AF-SVs. Their model suggests the presence of a MR effect with an upper limit of approximately 100%. However, a more direct way to understand spin transmission in AF MTJs is to perform a band-structure analysis. Figure 3 illustrates the band structure of bulk Mn_2Au and CdO, along with the density of states (DOS) and Fermi surface of Mn_2Au. At the Mn_2Au/CdO interface, where O bonded with Mn (as evidenced by the Mn-O distance of approximately 1.93 Å), the DOS of the interfacial Mn (of Mn_2Au) is obviously affected by the O atom (of CdO). Specifically, the partial DOS peaks of the ↑ spin of the *d* states of the interfacial Mn atom shift downward, while those of the ↓ spin shift upward and shrink significantly compared to the partial DOS of the Mn atoms in bulk Mn_2Au. Consequently, this change induces the enhanced spin polarization and magnetic moments (Table I) of the interfacial Mn atoms at the Fermi energy. Additionally, the inset in Fig. 3(c) shows the partial DOS of the interfacial Mn atoms, indicating that both *p* and *d* orbits contribute mainly to the ↑ spin, and the total DOS of the ↑ spin is approximately four times larger than that of the ↓ spin. According to Julliere's model [40], the MR should be approximately 250%, which is close to the calculated value in the AF MTJs with an S1 structure that have a thinner CdO barrier, but approximately one order of magnitude smaller than that of AF MTJs with thicker barriers [Figs. 1(a) and 1(b)].

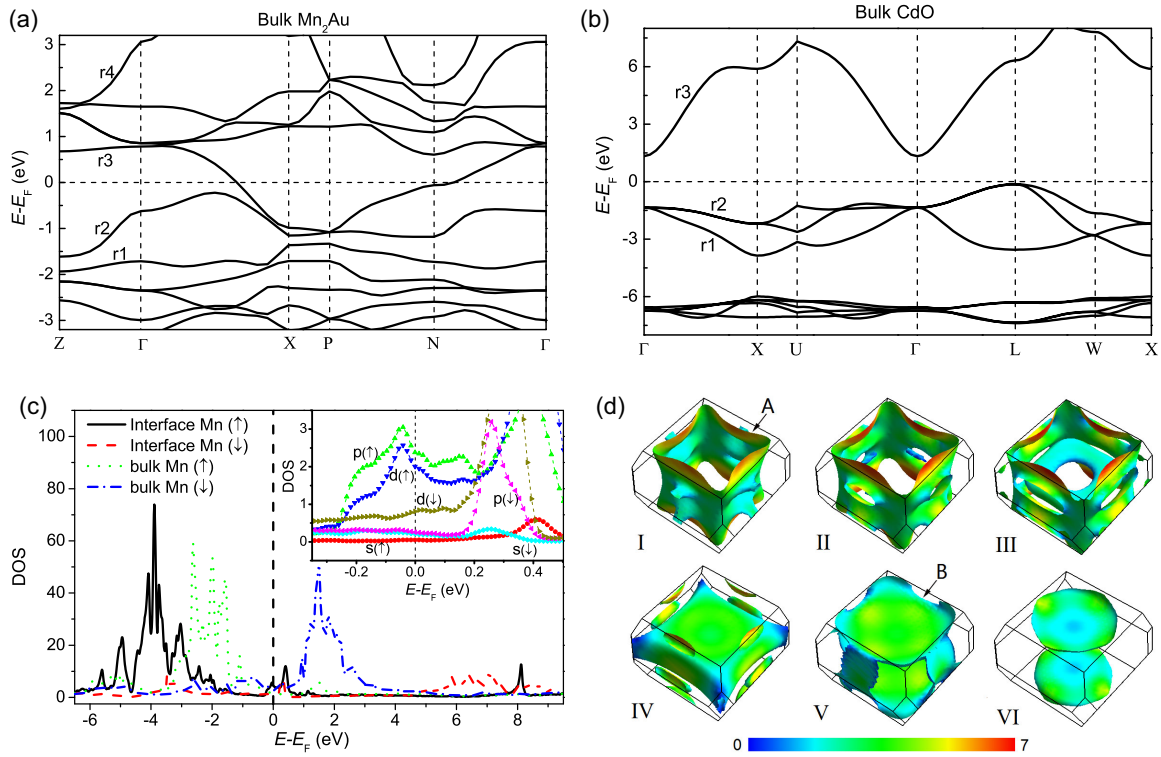

FIG. 3. Band structure of (a) tetragonal Mn_2Au and (b) rocksalt CdO in the first BZ of the primitive cell calculated using mBJ potential. (c) Density of states (DOS) of the bulk and interfacial Mn atoms with positive magnetic moment of the ideal Mn_2Au/CdO(10)/Mn_2Au multilayer. Inset of (c): partial DOS of the interfacial Mn atom. For the perpendicular structure of the multilayer, we pay attention to the bands in (a) with index r1, r2, r3, and r4 from the Γ (0 0 0) to Z (0.5 0.5 −0.5), and bands in (b) with index r1, r2, and r3 from the Γ to X (0.5 0 0.5) point. (d) Fermi surfaces FSs of tetragonal Mn_2Au around Fermi energy E_F, $E_F - 0.3$ eV, $E_F - 0.5$ eV, $E_F - 1.0$ eV, $E_F - 1.5$ eV, and $E_F - 1.7$ eV. The color bar indicates Fermi velocity in the Rydberg atomic unit. There are two FSs shown that range from E_F to $E_F - 1.7$ eV. The FS A present at E_F and disappearing around $E_F - 1.0$ eV is band r3 shown in (a), and the FS B appearing around $E_F - 0.3$ eV and disappearing around $E_F - 1.7$ eV is band r2 shown in (a).

For the $k_{||}$-resolved potential barrier nature of tetragonal Mn_2Au, the thickness of the barrier in Nb/Mn_2Au(24)/CdO(10)/Mn_2Au(24)/Nb AF-MTJ is dependent on the $k_{||}$ points. The thickness of the potential barrier is approximately 2.4 and 9.1 nm for $k_{||}$ points within and outside of the Sharvin area of Mn_2Au, respectively. Moreover, the band structure [Fig. 3(a)] suggests that $k_{||}$ points within or near the Sharvin area of Mn_2Au can perhaps satisfy the resonance condition, which should be responsible for the huge TMRs identified in AF MTJs with a thicker CdO barrier.

The complex band structure can be utilized to estimate tunnel transmission through a given barrier. Figure 4 presents the complex band structures of sandwiched CdO and bulk Mn_2Au at the 2D Γ point and a resonant $k_{||}$ point along the [001] direction. Obviously, bands with index r1, r2, and r3 in Fig. 4(a) are consistent with bands with index r1, r2, and r3 in Fig. 3(b), respectively, and bands with index r1, r2, r3, and r4 in Fig. 4(c) are consistent with bands with index r1, r2, r3, and r4 in Fig. 3(a), respectively. This indicates that the band structures calculated using the transport package [35] are consistent with that using the TB-LMTO codes [31]. Herein, we focus on bands with a smaller imaginary part near the Fermi energy. The symmetry of the imaginary bands can be estimated by the symmetry of the connected real bands. The crystal structure of rocksalt CdO is akin to that of MgO, and its complex band structure is similar to that of MgO. In Fig. 4(a), an imaginary Δ_1 band i1 connects with an s band [band r3 of Fig. 4(a)] and a d_{z^2} band [band r1 of Fig. 4(a)] at the Γ point, and an imaginary Δ_5 band i3 connects with the doubly degenerate bands d_{zx} and d_{zy} [band r2 of Fig. 4(a)]. The symmetry of the imaginary band i2 between i1 and i3 bands is difficult to identify. The imaginary band i1 has a smaller κ ($k = k_z + i\kappa$) in the vicinity of the Fermi energy, which would dominate tunneling transmission as the incoming electron has Δ_1 symmetry, indicating the potential symmetry filtering application shown in the Fe/MgO/Fe junction [23]. Furthermore, the semiconductor-type band gap and small effective mass at the Γ point [Fig. 3(b)] of CdO are favorable characteristics for spintronic applications.

The symmetry of the imaginary bands of tetragonal Mn_2Au is complex. There are two parabolic imaginary bands with Δ_1 symmetry as well as several irregular imaginary bands that are hard to identify directly, close to the Fermi energy. In Fig. 4(c), the imaginary Δ_1 band i3 is associated with real bands r2 and r4 at the Z point, and an adjacent imaginary Δ_1 band with larger κ (without marking here) is associated with the r1 and r3 bands at the Γ point. To determine the symmetry of the irregular bands marked as i1 and i2, particularly the band i1 with the smallest κ at the Fermi energy, the energy-dependent Fermi surface (FS) was studied [Fig. 3(d)].

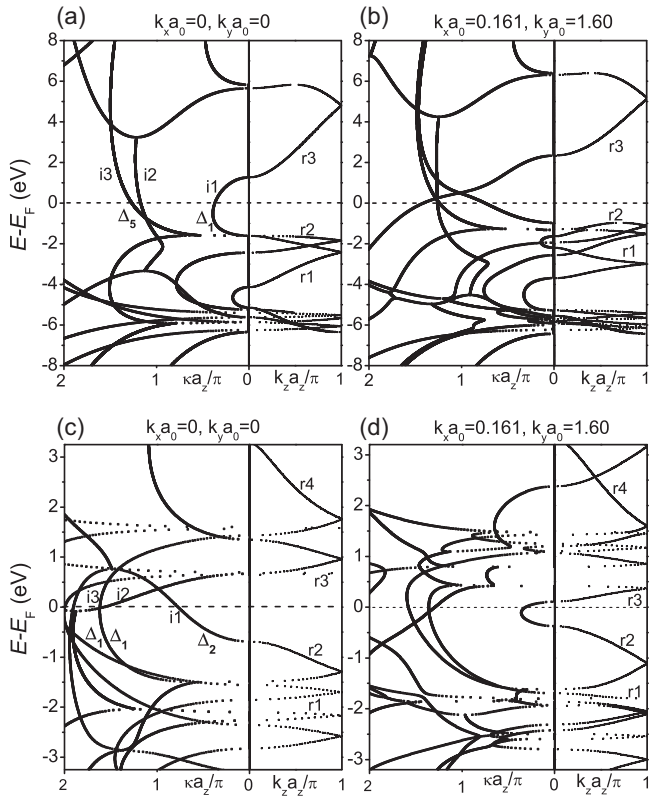

FIG. 4. Complex band structure of the sandwiched [(a) and (b)] CdO and [(c) and (d)] Mn_2Au in the Mn_2Au/CdO/Mn_2Au AF-MTJs at 2D Γ and one resonance $k_{||}$ points. Therein, k_z and κ are real and imaginary part of wave vector k, $a_0 = 3.328$ nm is the lateral lattice parameter, and a_z is the thickness of the repeat unit along the transport direction, which is 4.69 and 8.539 nm for CdO and Mn_2Au, respectively. Here, the real bands are folding.

This figure shows that the symmetry of both FS A and B is energy-dependent. The FS B displays four fragments located at approximately $\phi = 0°$, 90°, 180°, and 270° with d_{xy} (or $d_{x^2-y^2}$) symmetry at approximately $E_F - 0.3$ eV and an onion-ring structure at approximately $E_F - 0.5$ eV. The structure then transforms into a thin square drum with small gaps at each four corners around $E_F - 1.0$ eV. Subsequently, the square drum thickens and the gaps expand until two sheets situated parallel to the xy plane are formed around $E_F - 1.7$ eV. Within the energy range from $E_F - 1.0$ eV to $E_F - 1.7$ eV, the FS B can be identified as a combination of p_z and d_{z^2} symmetry. As the imaginary band i1 is associated with a d_{xy} orbit, it can be identified as having a Δ_2 symmetry.

At the Fermi energy, the electron is expected to decay with a rate of $\exp(-2\kappa\Delta_z)$, where Δ_z is the thickness of the barrier. According to the symmetry-filtering scheme proposed by Butler *et al.* [23], the bands can only accommodate incoming states with the same symmetry. Initially, we focus on the Δ_1 states. Along the transport direction, it can be estimated that κa_z is approximately 0.37π and 1.62π for the Δ_1 electrons of CdO and for the Δ_1 electrons of Mn_2Au, respectively. Assuming a symmetric AF-MTJ comprised of 24-Ls Mn_2Au and 10 Ls CdO, the tunneling transmission of the Δ_1 states at the 2D Γ point would be approximately 4.1×10^{-41} e^2/h. Assuming that the imaginary band i2 of CdO follows the same symmetry as the imaginary band i1 of Mn_2Au, its κa_z is 1.11π while that of the latter imaginary band is 0.67π. The spin transmission in the AF MTJs carried by the Δ_2 state would be approximately 1.7×10^{-30} e^2/h. In comparison, based on the scattering wave function, the transmission in the ideal Nb/Mn_2Au(24)/CdO(10)/Mn_2Au(24)/Nb AF MTJs with S1 structure is approximately 1.0×10^{-49} and 3.7×10^{-51} e^2/h for the P and AP magnetic states, respectively. Our calculations indicate that the imaginary Δ_1 band should be responsible for the spin transmission at the 2D Γ point. Furthermore, there are several effects that should be considered responsible for the notable difference between the model and first-principles calculations, including band alignments, band mismatch, interface scattering, and the mass of the electron entering into the barriers. For example, considering a band mismatch of 3.4 eV between the bulk Mn_2Au and CdO, the bands of the interfacial CdO would bend up, while that of the interfacial Mn_2Au would bend down, resulting in a Schottky barrier height of approximately 1.1 eV. Consequently, this barrier would not only change the barrier profile but also lead to noticeable spin-transport changes, especially when the barrier is ultrathin. Although the interfacial structure can be observed using the potential profile, quantitatively analyzing it is difficult.

For $k_{||}$ points located slightly away from the 2D Γ point with $|k_x| \leqslant \pi/100$ and $|k_y| \leqslant \pi/100$, the average spin transmissions for the P and AP magnetic states of the ideal Nb/Mn_2Au(24)/CdO(10)/Mn_2Au(24)/Nb AF MTJs with S1 structure were found to be approximately 1.2×10^{-29} and 2.3×10^{-33} e^2/h, respectively. These calculated values are approximately 20 orders of magnitude greater than the value at the 2D Γ point, which is in turn almost 10 orders of magnitude greater than the model estimation performed by the Δ_1 states. However, this value is close to the model estimation performed by the Δ_2 states (assuming that the imaginary band i2 of CdO follows a Δ_2 symmetry).

As the $k_{||}$ points move outward from the 2D Γ point, the $k_{||}$-dependent barrier height and the band gap of rocksalt CdO decrease for the joint of band r2 from Γ to X [Fig. 3(b)]. However, a similar effect is found in tetragonal Mn_2Au. When the interfaces of the AF MTJs are sufficiently clean, some $k_{||}$ points with appropriate barrier height may satisfy the resonant tunneling condition. When it comes to ideal Nb-lead AF MTJs, only the $k_{||}$ points within or near the Sharvin area of Mn_2Au can satisfy the resonant tunneling condition for thicker barrier junctions. For a resonant $k_{||}$ point within the Sharvin area of Mn_2Au with $k_x a_0 = 0.161$ and $k_y a_0 = 1.60$, as shown in Figs. 4(b) and 4(d), the imaginary part of the wave vector contributed by the d states is significantly smaller than that at the 2D Γ point, as shown in Figs. 4(a) and 4(c), respectively. Thus, the interfacial resonant tunneling is directly responsible for the huge TMR effect in AF MTJs with thicker CdO; however, the $k_{||}$-dependent band structure of the system is the intrinsic nature.

C. Voltage bias dependence of TMR

Another effect of the complex band structures in the Nb-lead AF MTJs is the voltage bias dependent TMR effect

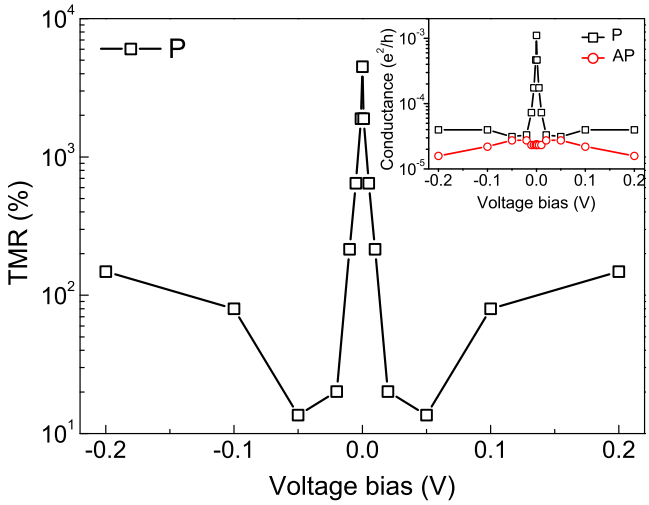

FIG. 5. Voltage bias-dependent TMRs and conductance in the ideal Nb/Mn_2Au(24)/CdO(10)/Mn_2Au(24)/Nb AF MTJs with S1 structure.

(Fig. 5). When a voltage bias is applied, the potentials in the CdO region shift linearly, while those in the Mn_2Au region remain unchanged due to its metallic nature. This potential shift affects the interfacial resonance [38], and hence spin transmissions in the ideal Nb/Mn_2Au(24)/CdO(10)/Mn_2Au(24)/Nb AF MTJs become sensitive to voltage bias. More specifically, a voltage bias of 0.001 V can reduce the spin transmission in the P magnetic state of the AF MTJs with an S1 structure by a factor of 20, as shown in the inset of Fig. 5. In contrast, the total transmission of the AP magnetic state of the AF MTJs is not so sensitive to the voltage bias. As a result, the TMR of the AF MTJs junction decreases from 4500% at the equilibrium state to 14% at a voltage bias of 0.05 V, and then increases to 150% at a voltage bias of 0.2 V.

Table II presents a summary of the conductances and TMRs of the ideal Nb/Mn_2Au(24)/CdO(10)/Mn_2Au(24)/Nb(001) AF MTJs at the equilibrium state and 0.1 V voltage bias. At the equilibrium state, the symmetric structures exhibited larger tunneling conductances and TMRs than the asymmetric ones. Among all the studied cases, the S1 structure exhibited the largest tunneling conductance, while the S3 structure exhibited the largest TMR. Under a voltage bias of 0.1 V, the tunneling conductances of the P and PP magnetic states of the symmetric structures S1 and S3 were found to be more sensitive to the voltage bias than the AP structure, leading to a sharp decrease in the TMR effect. The S2 structure was an exception among the symmetric structures, where both the tunnel conductances and TMRs were insensitive to a finite voltage bias. The P, PP, and AP magnetic states of the asymmetric structures A1 and A2 exhibited a similar behavior in the presence of voltage bias, with TMRs remaining insensitive to the voltage bias. The A3 structure was an exception among the asymmetric structures, with both the tunneling conductances and TMRs increasing under a finite voltage bias. Consequently, the tunneling conductance and TMR effect in the ideal Nb-lead AF MTJs exhibit a complex dependence on the magnetic structures, atomic structures, and voltage bias. These complex dependencies can be explained by the complex band structure of the CdO and Mn_2Au in conjunction with the localized magnetism at the Mn_2Au/CdO interface induced by interfacial effects, as discussed above.

D. Interfacial disorder

Experimental realization of an ideal heterostructure is challenging as imperfections are commonly present, which have a tendency to concentrate at the interfaces. Herein, we focused on three types of imperfections, which are comprehensively listed in Table II. Generally, the introduction of interfacial disorders can substantially degrade the interfacial resonance-tunneling effect between the same spin channels while simultaneously increasing the scattering probability among different spin channels [38]. Interfacial manganese vacancies have a greater impact on increasing the scattering probability among different spin channels compared to interfacial oxygen vacancies and manganese-cadmium (Mn-Cd) exchanges with the same concentration. At an equilibrium state, it has been observed that the presence of 10% interfacial imperfections can reduce the TMRs in the Nb/Mn_2Au(24)/CdO(10)/Mn_2Au(24)/Nb(001) AF-MTJs from several hundred percent in junctions with clean interfaces to the order of 1. To achieve a larger TMR effect, the interfaces of the AF-MTJs should be as clean as possible.

IV. SUMMARY

In summary, we used the first-principles scattering theory to calculate the spin transmission and TMR effect in all-AF Mn_2Au-based MTJs. Our findings reveal high TMRs in some symmetric junctions of the order of 1000%, while TMRs of around 100% were found in some asymmetric junctions. The interfacial resonance-tunneling effect was attributed to the high TMR effect, which was related to the $k_{||}$-dependent band structures of the system and the enhanced magnetism of the interface atoms. The TMR effect in the ideal all-AF MTJs was found to be sensitive to the interfacial structure, voltage bias, and interfacial disorder. For an ideal symmetric junction with an S1 structure comprising 24-Ls Mn_2Au and 10-Ls CdO, a voltage bias of 0.1 V could reduce the TMR from 4580% at the equilibrium state to 80%. Additionally, the introduction of a 10% interfacial disorder, such as O vacancies, Mn vacancies, and Mn–Cd exchanges at the Mn_2Au/CdO interface, could reduce TMRs in symmetric junctions with clean interfaces from several thousand percent to the order of 100%. The large TMR effect predicted in all-AF MTJs indicates the possibility for exploiting antiferromagnetism without the aid of FMs or ferrimagnets. Furthermore, rocksalt CdO can be considered a promising material for spintronic applications due to its good symmetry-filtering effect as well as its semiconductor-type band gap.

ACKNOWLEDGMENTS

We gratefully acknowledge the financial support received from the National Natural Science Foundation of China (Grants No. 12074102, No. 11804062, and No. 11804310). The authors acknowledge Prof. Yong Yang of ISSP of CAS for useful discussions.

[1] T. Jungwirth, X. Marti, P. Wadley, and J. Wunderlich, Nat. Nanotechnol. **11**, 231 (2016).

[2] V. Baltz, A. Manchon, M. Tsoi, T. Moriyama, T. Ono, and Y. Tserkovnyak, Rev. Mod. Phys. **90**, 015005 (2018).

[3] A. S. Núñez, R. A. Duine, P. Haney, and A. H. MacDonald, Phys. Rev. B **73**, 214426 (2006).

[4] X.-T. Jia, X.-L. Cai, and Y. Jia, Sci. China Phys. Mech. Astron. **63**, 297512 (2020).

[5] X. Jia, H. Tang, S. Wang, and M. Qin, Phys. Rev. B **95**, 064402 (2017).

[6] Y. Zhu, X. Y. Guo, L. N. Jiang, Z. R. Yan, Y. Yan, and X. F. Han, Phys. Rev. B **103**, 134437 (2021).

[7] Z. Yan, R. Zhang, X. Dong, S. Qi, and X. Xu, Phys. Chem. Chem. Phys. **22**, 14773 (2020).

[8] X. Guo, B. Yang, X. Zhang, Y. Zhu, X. Han, and Y. Yan, Phys. Rev. B **104**, 144423 (2021).

[9] J. Yang, S. Fang, Y. Peng, S. Liu, B. Wu, R. Quhe, S. Ding, C. Yang, J. Ma, B. Shi *et al.*, Phys. Rev. Appl. **16**, 024011 (2021).

[10] B. Wu, J. Yang, R. Quhe, S. Liu, C. Yang, Q. Li, J. Ma, Y. Peng, S. Fang, J. Shi *et al.*, Phys. Rev. Appl. **17**, 034030 (2022).

[11] X. Li, J.-T. Lü, J. Zhang, L. You, Y. Su, and E. Y. Tsymbal, Nano Lett. **19**, 5133 (2019).

[12] H. Yang, Q. Liu, Z. Liao, L. Si, P. Jiang, X. Liu, Y. Guo, J. Yin, M. Wang, Z. Sheng *et al.*, Phys. Rev. B **104**, 214419 (2021).

[13] J. Dong, X. Li, G. Gurung, M. Zhu, P. Zhang, F. Zheng, E. Y. Tsymbal, and J. Zhang, Phys. Rev. Lett. **128**, 197201 (2022).

[14] P. Qin, H. Yan, X. Wang, H. Chen, Z. Meng, J. Dong, M. Zhu, J. Cai, Z. Feng, X. Zhou, L. Liu, T. Zhang, Z. Zeng, J. Zhang, C. Jiang, and Z. Liu, Nature (London) **613**, 485 (2023).

[15] L. Šmejkal, A. B. Hellenes, R. González-Hernández, J. Sinova, and T. Jungwirth, Phys. Rev. X **12**, 011028 (2022).

[16] C. Song, Y. You, X. Chen, X. Zhou, Y. Wang, and F. Pan, Nanotechnology **29**, 112001 (2018).

[17] E. V. Gomonay and V. M. Loktev, Low Temp. Phys. **40**, 17 (2014).

[18] P. Wadley, B. Howells, J. Železný, C. Andrews, V. Hills, R. P. Campion, V. Novák, K. Olejník, F. Maccherozzi, S. S. Dhesi *et al.*, Science **351**, 587 (2016).

[19] S. Y. Bodnar, L. Šmejkal, I. Turek, T. Jungwirth, O. Gomonay, J. Sinova, A. Sapozhnik, H.-J. Elmers, M. Kläui, and M. Jourdan, Nat. Commun. **9**, 348 (2018).

[20] N. Bhattacharjee, A. A. Sapozhnik, S. Y. Bodnar, V. Y. Grigorev, S. Y. Agustsson, J. Cao, D. Dominko, M. Obergfell, O. Gomonay, J. Sinova *et al.*, Phys. Rev. Lett. **120**, 237201 (2018).

[21] X. F. Zhou, J. Zhang, F. Li, X. Z. Chen, G. Y. Shi, Y. Z. Tan, Y. D. Gu, M. S. Saleem, H. Q. Wu, F. Pan *et al.*, Phys. Rev. Appl. **9**, 054028 (2018).

[22] Y. Deng, X. Liu, Y. Chen, Z. Du, N. Jiang, C. Shen, E. Zhang, H. Zheng, H.-Z. Lu, and K. Wang, Natl. Sci. Rev. **10**, nwac154 (2022).

[23] W. H. Butler, X.-G. Zhang, T. C. Schulthess, and J. M. MacLaren, Phys. Rev. B **63**, 054416 (2001).

[24] J. Mathon and A. Umerski, Phys. Rev. B **63**, 220403(R) (2001).

[25] S. Ikeda, K. Miura, H. Yamamoto, K. Mizunuma, H. Gan, M. Endo, S. Kanai, J. Hayakawa, F. Matsukura, and H. Ohno, Nat. Mater. **9**, 721 (2010).

[26] X.-T. Jia, X.-L. Cai, W.-Y. Yu, L.-W. Zhang, B.-J. Wang, G.-H. Cao, S.-Z. Wang, H.-M. Tang, and Y. Jia, J. Phys. D **53**, 245001 (2020).

[27] X. F. Zhou, X. Z. Chen, J. Zhang, F. Li, G. Y. Shi, Y. M. Sun, M. S. Saleem, Y. F. You, F. Pan, and C. Song, Phys. Rev. Appl. **11**, 054030 (2019).

[28] P. N. Hai, J. Magn. Soc. Jpn. **44**, 137 (2020).

[29] V. Barthem, C. Colin, H. Mayaffre, M.-H. Julien, and D. Givord, Nat. Commun. **4**, 2892 (2013).

[30] G. Kresse and J. Furthmüller, Phys. Rev. B **54**, 11169 (1996).

[31] I. Turek, V. Drchal, J. Kudrnovský, M. Sob, and P. Weinberger, *Electronic Structure of Disordered Alloys, Surfaces and Interfaces* (Kluwer, Boston, 1997).

[32] F. Tran and P. Blaha, Phys. Rev. Lett. **102**, 226401 (2009).

[33] X. Liu, C. Li, S. Han, J. Han, and C. Zhou, Appl. Phys. Lett. **82**, 1950 (2003).

[34] R. Chandiramouli and B. Jeyaprakash, Solid State Sci. **16**, 102 (2013).

[35] S. Wang, Y. Xu, and K. Xia, Phys. Rev. B **77**, 184430 (2008).

[36] Y. Ke, K. Xia, and H. Guo, Phys. Rev. Lett. **100**, 166805 (2008).

[37] A. B. Shick, S. Khmelevskyi, O. N. Mryasov, J. Wunderlich, and T. Jungwirth, Phys. Rev. B **81**, 212409 (2010).

[38] Y. Ke, K. Xia, and H. Guo, Phys. Rev. Lett. **105**, 236801 (2010).

[39] X. Jia, K. Xia, and G. E. W. Bauer, Phys. Rev. Lett. **107**, 176603 (2011).

[40] M. Julliere, Phys. Lett. A **54**, 225 (1975).